JOURNAL OF COMPUTATIONAL PHYSICS **63**, 107–129 (1986)

Numerical Calculations Using the Full MHD Equations in Toroidal Geometry*

L. A. CHARLTON, J. A. HOLMES, H. R. HICKS,
V. E. LYNCH, AND B. A. CARRERAS

Oak Ridge National Laboratory, Oak Ridge, Tennessee 37831

Received September 18, 1984; revised April 26, 1985

A computer code has been constructed that solves the full magnetohydronamic (MHD) equations in toroidal geometry. The code is applicable to toroidal devices, including tokamaks, stellarators, and reversed field pinches. A fully implicit numerical technique is used that allows linear eigenvalues and eigenfunctions to be found in a very few computational steps. Althought the present work dscribes the solution of the linearized equations, generalization of the numerical method to the solution of the nonlinear problem is straightforward. Use of the code is illustrated by calculating the $n = 1$ instability for a tokamak configuration. The results show the structural changes in the eigenfunctions as the plasma pressure is increased.

I. INTRODUCTION

A formalism to solve the magnetohydrodynamic (MHD) equations in toroidal geometry has been developed which follows very closely that devised in Ref [1]. This approach uses the full MHD equations with no ordering assumptions. The fluid is assumed to be incompressible. Both ideal and resistive modes can be studied. A computer code FAR has been constructed to solve these equations using a fully implicit scheme. Extensive research using the full MHD equations in nontoroidal geometries has been carried out by Schnack and Killeen [2], Hender [3], Aydemir and Barnes [4], and Izzo *et al.* [5].

At present the FAR code can be used to study the linear stability of plasmas in toroidal devices, such as tokamaks, reversed field pinches, and stellarators (using the stellarator expansion approach). The extension of the numerical technique to the solution of the nonlinear equations is straightforward and is being pursued. In the present paper we limit the discussion to the tokamak configuration. The fully implicit nature of the numerics allows extremely fast linear calculations, as will be discussed. The speed is accomplished by exploiting the resonant behavior of the implicit scheme. When a reasonable guess for the eigenvalue is known, convergence can be achieved in a few steps. It is also possible to study unstable modes other

---

*Research sponsored by the Office of Fusion Energy, U.S. Department of Energy, under Contract DE-AC05-84OR21400 with Martin Marietta Energy Systems, Inc.

0021-9991/86 $3.00

than the most unstable one by properly choosing the step-size convergence parameter. Numerical results for resistive $n=1$ tokamak instabilities have been compared with the results of the computer code RST [6], which solves a reduced set of MHD equations based on large aspect ratio tokamak ordering [7]. In the cylindrical limit, $n=1$ results have been compared with those of CYL [8], an initial value code that solves the full MHD equations in cylindrical geometry. Detailed comparisons of ideal tokamak instabilities have also been made with the results of ERATO [9], which solves the compressible MHD equations in the ideal limit with a δW approach.

In Section 2, the equations and their derivations will be discussed. The boundary conditions are discussed in Section 3, and numerical techniques presented in Section 4. Results to illustrate the numerical behavior and use of the code are given in Section 5. Discussion and conclusions are presented in Section 6.

II. EQUATIONS

Let us consider the resistive MHD equations,

$$\frac{\partial \mathbf{B}}{\partial t} = -\nabla \times \mathbf{E}, \tag{1}$$

$$\mathbf{E} + \mathbf{v} \times \mathbf{B} = \eta \mathbf{J}, \tag{2}$$

$$\rho_m \left(\frac{\partial \mathbf{v}}{\partial t} + \mathbf{v} \cdot \nabla \mathbf{v} \right) = -\nabla p + \mathbf{J} \times \mathbf{B}, \tag{3}$$

$$\mathbf{J} = \nabla \times \mathbf{B}, \tag{4}$$

$$\nabla \cdot \mathbf{B} = 0, \tag{5}$$

$$\frac{\partial p}{\partial t} + \mathbf{v} \cdot \nabla p + \Gamma p \nabla \cdot \mathbf{v} = 0, \tag{6}$$

and

$$\frac{\partial \rho_m}{\partial t} + \nabla \cdot (\rho_m \mathbf{v}) = 0. \tag{7}$$

In this work we shall make the simplifying assumptions that the fluid velocity obey the condition

$$\nabla \cdot \frac{\mathbf{v}}{R^2} = 0, \tag{8}$$

and that the mass density ρ_m be constant in time. The velocity constraint reduces to incompressibility in cylindrical geometry. In toroidal geometry, the correction $1/R^2$

leads to a convenient representation in terms of potential functions while suppressing compressional Alfvén waves. Strictly speaking, this assumption restricts the domain of applicability to phenomena in which compressibility is not an important effect. For kink modes the effects omitted by an incompressibility assumption are small as shown in Section V where a comparison is made with the MHD stability code ERATO [9] which includes such effects. Work is underway, however, to add the effects of compressibility to the present code since they may be important in the study of ballooning modes [10]. The constraint on the mass density implies

$$\nabla \cdot (\rho_m \mathbf{v}) = 0. \tag{9}$$

It is consistent with the above constraints to assume for the equilibrium mass density the following form:

$$\rho_m = \rho_m^0 \left(\frac{R_0}{R}\right)^2, \tag{10}$$

where R is the major radius and R_0 is its value at the magnetic axis.

The MHD equations are solved in toroidal geometry. An equilibrium flux coordinate system (ρ, θ, ζ) [6] is used, where ρ is a flux surface label, θ is a generalized poloidal angle variable, and ζ is the toroidal angle. The angle θ is determined from the straight magnetic field line condition. Equations (1)–(10) can be written in terms of potential functions that guarantee an exact solution of Eq. (5) and the incompressibility condition (8). For the magnetic field the usual vector potential

$$\mathbf{B} = \nabla \times \mathbf{A} \tag{11}$$

is used together with the gauge condition $A_\rho = 0$. This choice of gauge allows the remaining two covariant components of the vector potential to be identified with the poloidal and toroidal magnetic fluxes. The velocity is treated in similar fashion. Defining a velocity potential $\mathbf{\Omega}$ to obey the equation

$$\frac{\mathbf{v}}{R^2} = \nabla \times \mathbf{\Omega} \tag{12}$$

the velocity "gauge" condition $\Omega_\rho = 0$ is chosen. Of the remaining components, Ω_ζ is the velocity stream function and Ω_θ is closely related to the toroidal velocity. Using these potentials, Eqs. (5) and (8) are obeyed identically.

We now express Eqs. (1)–(10) in terms of the potentials defined in Eqs. (11) and (12). Equations (7) and (9) may be disregarded because of the incompressibility assumption [Eq. (8)] and the assumed form of the mass density [Eq. (10)]. Faraday's law (1) and Ohm's law (2) can be combined to derive the time evolution equation for $\mathbf{A}$,

$$\frac{\partial \mathbf{A}}{\partial t} = \mathbf{v} \times \mathbf{B} - \eta \mathbf{J} + \nabla \alpha, \tag{13}$$

where α is the negative of the electrostatic potential. To express the moment equation in terms of the velocity potential and the vorticity

$$\mathbf{U} = R^2\nabla \times \mathbf{v}, \tag{14}$$

we apply the operator $\nabla \times R^2$ to Eq. (3). Expressing the above in terms of the generalized coordinates (ρ, θ, ζ) leads to six equations for six unknowns. These equations are

$$\frac{\partial\psi}{\partial t} = -\frac{\partial\alpha}{\partial\zeta} - v^\rho B^\theta + v^\theta B^\rho + \eta j_\zeta - E_\zeta, \tag{15}$$

$$\frac{\partial\chi}{\partial t} = -\frac{1}{\rho}\frac{\partial\alpha}{\partial\theta} - v^\zeta B^\rho + v^\rho B^\zeta + \eta j_\theta, \tag{16}$$

$$\frac{\partial\alpha}{\partial\rho} = -v^\theta B^\zeta + v^\zeta B^\theta + \eta j_\rho, \tag{17}$$

$$\begin{aligned}\frac{\partial U^\theta}{\partial t} = {} & \frac{\partial}{\partial\zeta}(v^\theta U^\zeta - v^\zeta U^\theta) + \frac{\partial}{\partial\rho}(v^\theta U^\rho - v^\rho U^\theta) \\ & + S^2\left[-\frac{\beta_0}{2\varepsilon^2}\left(\frac{\partial R^2}{\partial\zeta}\frac{\partial p}{\partial\rho} - \frac{\partial R^2}{\partial\rho}\frac{\partial p}{\partial\zeta}\right)\right. \\ & \left. + \frac{\partial}{\partial\zeta}(j^\theta B^\zeta - j^\zeta B^\theta) + \frac{\partial}{\partial\rho}(j^\theta B^\rho - j^\rho B^\theta)\right],\end{aligned} \tag{18}$$

$$\begin{aligned}\frac{\partial U^\zeta}{\partial t} = {} & \frac{1}{\rho}\frac{\partial}{\partial\rho}[\rho(v^\zeta U^\rho - v^\rho U^\zeta)] + \frac{1}{\rho}\frac{\partial}{\partial\theta}(v^\zeta U^\theta - v^\theta U^\zeta) \\ & + S^2\left\{-\frac{\beta_0}{2\varepsilon^2}\left(\frac{\partial R^2}{\partial\rho}\frac{1}{\rho}\frac{\partial p}{\partial\theta} - \frac{1}{\rho}\frac{\partial R^2}{\partial\theta}\frac{\partial p}{\partial\rho}\right)\right. \\ & \left. + \frac{1}{\rho}\frac{\partial}{\partial\rho}[\rho(j^\zeta B^\rho - j^\rho B^\zeta)] + \frac{1}{\rho}\frac{\partial}{\partial\theta}(j^\zeta B^\theta - j^\theta B^\zeta)\right\},\end{aligned} \tag{19}$$

and

$$\begin{aligned}\frac{\partial p}{\partial t} = {} & -v^\rho\left(\frac{\partial p}{\partial\rho} + \Gamma\frac{R}{R^2}\frac{\partial R^2}{\partial\rho}\right) \\ & - v^\theta\left(\frac{1}{\rho}\frac{\partial p}{\partial\theta} + \Gamma p\frac{1}{\rho R^2}\frac{\partial R^2}{\partial\theta}\right) \\ & - v^\zeta\left(\frac{\partial p}{\partial\zeta} + \Gamma\frac{p}{R^2}\frac{\partial R^2}{\partial\zeta}\right).\end{aligned} \tag{20}$$

The six unknowns are the poloidal flux function $\psi = -A_\zeta$, the toroidal flux function $\chi = -A_\theta$, the poloidal velocity stream function $\phi = -\Omega_\zeta$, the toroidal velocity stream function $\Lambda = -\Omega_\theta$, the electrostatic potential α, and the pressure p. In terms of these quantities, the magnetic field and velocity, respectively, are given by

$$\mathbf{B} = \nabla\theta \times \nabla(\rho\chi) + \nabla\zeta \times \nabla\psi \tag{21}$$

and

$$\mathbf{v} = R^2[\nabla\theta \times \nabla(\rho\Lambda) + \nabla\zeta \times \nabla\phi]. \tag{22}$$

Specifically, the quantities that appear in the equations to be time advanced [Eqs. (15)–(20)] are related to the six unknowns by

$$\mathrm{v}^\rho = -\left(\frac{1}{\rho}\frac{\partial\phi}{\partial\theta} - \frac{\partial\Lambda}{\partial\zeta}\right), \tag{23}$$

$$v^\theta = \frac{\partial\phi}{\partial\rho}, \tag{24}$$

$$v^\zeta = -\frac{1}{\rho}\frac{\partial(\rho\Lambda)}{\partial\rho}, \tag{25}$$

$$B^\rho = -\left(\frac{1}{\rho}\frac{\partial\psi}{\partial\theta} - \frac{\partial\chi}{\partial\zeta}\right), \tag{26}$$

$$B^\theta = \frac{\partial\psi}{\partial\rho}, \tag{27}$$

$$B^\zeta = -\frac{1}{\rho}\frac{\partial(\rho\chi)}{\partial\rho}, \tag{28}$$

$$j_\rho = -\left(g^{\theta\theta}\frac{1}{\rho}\frac{\partial}{\partial\theta} + g^{\rho\theta}\frac{\partial}{\partial\rho}\right)\left[\frac{1}{\rho}\frac{\partial(\rho\chi)}{\partial\rho}\right] - \frac{\varepsilon^2}{R^2}\frac{\partial^2\psi}{\partial\zeta\partial\rho}, \tag{29}$$

$$\begin{aligned} j_\theta = {} & \left(g^{\rho\rho}\frac{\partial}{\partial\rho} + g^{\rho\theta}\frac{1}{\rho}\frac{\partial}{\partial\theta}\right)\left[\frac{1}{\rho}\frac{\partial(\rho\chi)}{\partial\rho}\right] \\ & - \frac{\varepsilon^2}{R^2}\frac{\partial}{\partial\zeta}\left(\frac{1}{\rho}\frac{\partial\psi}{\partial\theta} - \frac{\partial\chi}{\partial\zeta}\right), \end{aligned} \tag{30}$$

$$\begin{aligned} j_\zeta = {} & \frac{1}{\rho}\frac{\partial}{\partial\rho}\left(g^{\rho\rho}\frac{\rho\partial\psi}{\partial\rho}\right) + \frac{1}{\rho}\frac{\partial}{\partial\rho}\left[g^{\rho\theta}\rho\left(\frac{1}{\rho}\frac{\partial\psi}{\partial\theta} - \frac{\partial\chi}{\partial\zeta}\right)\right] \\ & + \frac{1}{\rho}\frac{\partial}{\partial\theta}\left[g^{\theta\theta}\left(\frac{1}{\rho}\frac{\partial\psi}{\partial\theta} - \frac{\partial\chi}{\partial\zeta}\right)\right] \\ & + \frac{1}{\rho}\frac{\partial}{\partial\theta}\left(g^{\rho\theta}\frac{\partial\psi}{\partial\rho}\right), \end{aligned} \tag{31}$$

$$U^{\rho}=\frac{-1}{\varepsilon^2}\frac{1}{\rho}\frac{\partial}{\partial\theta}\left[\frac{R^2}{\rho}\frac{\partial}{\partial\rho}(\rho\Lambda)\right]-\frac{\partial}{\partial\zeta}\left[R^2g^{\rho\theta}\left(\frac{1}{\rho}\frac{\partial\phi}{\partial\theta}-\frac{\partial\Lambda}{\partial\zeta}\right)\right]$$
$$-\frac{\partial}{\partial\zeta}\left(R^2g^{\rho\rho}\frac{\partial\phi}{\partial\rho}\right), \tag{32}$$

$$U^{\theta}=\frac{1}{\varepsilon^2}\frac{\partial}{\partial\rho}\left[R^2\frac{1}{\rho}\frac{\partial(\rho\Lambda)}{\partial\rho}\right]$$
$$-\frac{\partial}{\partial\zeta}\left[R^2g^{\theta\theta}\left(\frac{1}{\rho}\frac{\partial\phi}{\partial\theta}-\frac{\partial\Lambda}{\partial\zeta}\right)\right]$$
$$-\frac{\partial}{\partial\zeta}\left(R^2g^{\rho\theta}\frac{\partial\phi}{\partial\rho}\right), \tag{33}$$

and

$$U^{\zeta}=\frac{1}{\rho}\frac{\partial}{\partial\rho}\left(R^2g^{\rho\rho}\frac{\rho\partial\phi}{\partial\rho}\right)+\frac{1}{\rho}\frac{\partial}{\partial\rho}\left[R^2g^{\rho\theta}\rho\left(\frac{1}{\rho}\frac{\partial\phi}{\partial\theta}-\frac{\partial\Lambda}{\partial\zeta}\right)\right]$$
$$+\frac{1}{\rho}\frac{\partial}{\partial\theta}\left(R^2g^{\rho\theta}\frac{\partial\phi}{\partial\rho}\right)+\frac{1}{\rho}\frac{\partial}{\partial\theta}\left[R^2g^{\theta\theta}\left(\frac{1}{\rho}\frac{\partial\phi}{\partial\theta}-\frac{\partial\Lambda}{\partial\zeta}\right)\right]. \tag{34}$$

In Eqs. (15)–(34), all lengths are normalized to a generalized minor radius a [defined by $a^2=R_0\int R^{-2}dV/(2\pi^2)$, with the integration over the plasma volume]; the resistivity to η_0 (its value at the magnetic axis); the time to the resistive diffusion time $\tau_r=a^2\mu_0/\eta_0$, where μ_0 is the vacuum magnetic permeability; the magnetic field to B_0 (the toroidal vacuum field at the plasma major radius R_0); the velocity to a/τ_r, and the pressure to p_0 (its equilibrium value at the magnetic axis). R is the major radius coordinate normalized to R_0, and $S=\tau_r/\tau_{Hp}$ is the ratio of the resistive time to the poloidal Alfvén time $[\tau_{Hp}=R_0(\mu_0\rho_m)^{1/2}/B_{\zeta 0}]$.

To solve this system of equations, the unknown quantities (X) are separated into equilibrium (X_{eq}) and perturbation ($\tilde{X}$) parts:

$$X(\rho,\theta,\zeta)=X_{\text{eq}}(\rho,\theta)+\tilde{X}(\rho,\theta,\zeta). \tag{35}$$

The purely equilibrium terms are discarded in FAR, leaving only terms that are linear or quadratic in the perturbed quantities. Only the linear version is discussed here.

For axisymmetric equilibria, without flows, Eqs. (15)–(20) lead to the following relations. From Eq. (15) we have

$$\eta\langle j_\zeta\rangle_{\text{eq}}=\langle E_\zeta\rangle_{\text{eq}} \tag{36}$$

where $\langle j_\zeta\rangle_{\text{eq}}$ and $\langle E_\zeta\rangle_{\text{eq}}$ are the flux-surface-averaged toroidal current and toroidal electric field, respectively. In the case of a tokamak, $\langle E_\zeta\rangle_{\text{eq}}$ is constant and is simply related to the voltage applied at the limiter. In equilibrium, Eqs. (18) and

(20) reduce identically to zero, while Eq. (19) becomes the Grad–Shafranov equation

$$(j^{\zeta}B^{\theta}-j^{\theta}B^{\zeta})_{\mathrm{eq}}=-\frac{\beta_0}{2\varepsilon^2}R^2\frac{dp_{\mathrm{eq}}}{d\rho}. \tag{37}$$

Finally, Eqs. (16) and (17) reduce to an equation for α

$$\nabla_{\perp}\alpha_{\mathrm{eq}}=\eta\mathbf{j}_{\perp\mathrm{eq}}. \tag{38}$$

This equation can be solved in general only in the ideal case ($\eta=0\Rightarrow\alpha_{\mathrm{eq}}=\text{constant}$). Therefore, this system of equations gives an ideal, axisymmetric equilibrium solution for the tokamak configuration. In terms of the variables we have introduced, this solution can be written as

$$\chi_{\mathrm{eq}}=-\frac{1}{\rho}\int_0^{\rho}d\rho\,\rho F_{\mathrm{eq}}(\rho), \tag{39}$$

where $F_{\mathrm{eq}}(\rho)$ is the toroidal flux function,

$$\psi_{\mathrm{eq}}=-\int d\rho\,\rho\frac{F_{\mathrm{eq}}(\rho)}{q(\rho)}, \tag{40}$$

and $\alpha_{\mathrm{eq}}=\Lambda_{\mathrm{eq}}=\Lambda_{\mathrm{eq}}=0$. We assume the equilibrium pressure is a given function $p_{\mathrm{eq}}(\rho)$. We can either specify $F(\rho)$ or $q(\rho)$ to determine a complete tokamak equilibrium solution.

At large aspect ratio, using the tokamak ordering, $\tilde{B}^{\zeta}$ and $\tilde{v}^{\zeta}$ can be neglected compared to the magnetic and fluid perturbations perpendicular to the toroidal field. Furthermore, to lowest order in ε, $B^{\zeta}\sim$constant. Therefore, to the lowest order in this limit, $\tilde{\Lambda}$ and $\tilde{\chi}$ can be neglected and

$$\tilde{\alpha}\simeq -R_0B_0\tilde{\phi}.$$

Equations (16), (17), and (18) are then trivially verified, and Eqs. (15), (19), and (20) are equivalent to the reduced set of resistive MHD equations derived by Strauss [7].

To solve Eqs. (15)–(20), the perturbed quantities are expanded in Fourier series using the approach described in Ref. [11]. Assuming up–down symmetry of the equilibrium, the perturbed quantities $\tilde{\psi}$, $\tilde{p}$, and $\tilde{\chi}$ can be expanded in cosine functions,

$$\tilde{X}(\rho,\theta,\zeta)=\sum_{m,n}\tilde{X}_{mn}(\rho)\cos(m\theta+n\zeta), \tag{41}$$

and $\tilde{\phi}$, $\tilde{\Lambda}$, and $\tilde{\alpha}$ in sine functions

$$\tilde{X}(\rho,\theta,\zeta)=\sum_{m,n}\tilde{X}_{mn}(\rho)\sin(m\theta+n\zeta). \tag{42}$$

Here, n is the toroidal wave number and m is the poloidal wave number, and the $\sum_{m,n}$ is taken over $n>0$ for all m and over $n=0$ for $m \geqslant 0$.

For a numerical solution, Eqs. (15)–(20) are written in terms of ψ, χ, ϕ, Λ, p, and the quantity

$$\alpha^* = \alpha - \frac{1}{\rho}\frac{\partial}{\partial \rho}(\rho \chi_{\text{eq}})\,\Phi + \frac{\partial}{\partial \rho}\,\Psi_{\text{eq}}\Lambda$$

rather than α. This substitution simplifies some of the terms involved in the matrix solution of these equations. From this point on α^* will be referred to as α.

III. BOUNDARY CONDITIONS

In this section the behavior of the solutions near the magnetic axis and at the plasma edge is discussed. The conditions at the magnetic axis are determined by requiring that the physical quantities be "well behaved" (i.e., that none of the fields, nor the fields obtained from them by applying standard vector operators, have singularities at the origin). In the generalized toroidal coordinates used here, this means that for scalar fields (such as the pressure p and electrostatic potential α) and for the toroidal components of vector fields (such as $\psi = -A_\zeta$ and $\phi = -\Omega_\zeta$) the $(m; n)$ harmonics must approach the coordinate origin as either odd or even power series in ρ. For example,

$$\psi_{mn} = \rho^{|m|} \sum_{k=0}^{\infty} a_{2k}\rho^{2k}. \tag{43}$$

For the poloidal components of vector fields, such as $\chi = -A_\theta$ and $\Lambda = -\Omega_\theta$, the origin conditions take the form for χ of

$$\chi_{mn} = \rho^{||m|-1|} \sum_{k=0}^{\infty} a_{2k}\rho^{2k} \tag{44}$$

with the additional constraint that for $m \neq 0$ the leading terms of the ρ and θ components satisfy the relation

$$(a_0)_\rho = \pm \frac{m}{|m|}(a_0)_\theta. \tag{45}$$

Here the + sign is used when the θ component has a cosine series (χ) and the − sign is used when the θ component has a sine series (Λ).

Equations (43)–(45) summarize the behavior of scalar and vector fields at the magnetic axis in toroidal coordinates. In this work the scalar fields p and α and the toroidal vector fields ψ and ϕ are taken to satisfy Eq. (43). However, since only the gradients of the potential function α appear in the dynamical equations, we choose to require $\alpha = 0$ at the magnetic axis. This means that the leading term in Eq. (43) for $\alpha_{(m=0;n)}$ is given by a_2, with $a_0 = 0$. The motivation for this choice of origin condition for α is to allow a common treatment of all components in the solution of the α equation ($\alpha = 0$ at $\rho = 0$). The poloidal vector fields χ and Λ are taken to satisfy Eqs. (44) and (45). It is seen here that the gauge conditions $\Lambda_\rho = 0$ and $\Omega_\rho = 0$ imply, together with Eq. (45), that for $m \neq 0$ $a_0 = 0$ in Eq. (44). Hence, $\chi_{mn} \sim \rho^{|m|+1}$ and $\Lambda_{mn} \sim \rho^{|m|+1}$ as $\rho \to 0$.

A perfect conducting wall boundary condition is assumed at the plasma edge ($\rho = a$). This implies the following boundary conditions:

$$B^\rho|_{\rho=a} = v^\rho|_{\rho=a} = 0. \tag{46}$$

These are satisfied by requiring

$$m\psi_{mn} = n\chi_{mn} \tag{47}$$

and

$$m\phi_{mn} = n\Lambda_{mn} \tag{48}$$

at $\rho = a$. The edge values for ψ and χ are time advanced by

$$\left.\frac{\partial\psi}{\partial t}\right|_{\rho=a} = \left[-\frac{F_{\text{eq}}}{q}\left(\frac{\partial}{\partial\theta} - q\frac{\partial}{\partial\zeta}\right)\phi - \frac{\partial\alpha}{\partial\zeta}\right]_{\rho=a} \tag{49}$$

and

$$\left.\frac{\partial\chi}{\partial t}\right|_{\rho=a} = \left[-\frac{F_{\text{eq}}}{q}\left(\frac{\partial}{\partial\theta} - q\frac{\partial}{\partial\zeta}\right)\Lambda - \frac{\partial\alpha}{\partial\theta}\right]_{\rho=a}. \tag{50}$$

Equations (49) and (50) are simply Eqs. (15) and (16) written at $\rho = a$ using the conducting wall assumption $\tilde{j}_\zeta|_{\rho=a} = \tilde{j}_\theta|_{\rho=a} = 0$. We also assume that the perturbed pressure is zero at the edge:

$$\tilde{p}|_{\rho=a} = 0. \tag{51}$$

Finally, since α is the solution of a first-order equation, its value at the plasma edge is determined by extrapolation.

IV. NUMERICAL SCHEME

The linearization of Eqs. (15)–(20) can be written compactly as follows:

$$L\frac{\partial\tilde{X}}{\partial t} = R\tilde{X}, \tag{52}$$

where L and R are second-order spatial differential operators applied to the solution vector $\tilde{X}=(\tilde{\psi}, \tilde{\chi}, \tilde{\alpha}, \tilde{\Lambda}, \tilde{\phi}, \tilde{p})$. Assuming the spatial representation of Eqs. (41) and (42), Eq. (52) can be modeled as a finite difference problem by truncating the summations to include a finite mode selection and using a finite difference representation in the radial coordinate ρ. We use a three-point centered spatial finite difference scheme with variable mesh size to represent the radial problem [11]. In this representation, Eq. (52) takes the form of a finite matrix problem.

In cylindrical geometry, the problem decouples into separate independent matrices for each poloidal and toroidal mode number $(m; n)$: $L_{mn}(\partial \tilde{X}_{mn}/\partial t) = R_{mn}\tilde{X}_{mn}$. The matrices L_{mn} and R_{mn} are block tridiagonal. Each row of blocks consists of three 6×6 matrices (for the six unknowns), which represent the difference equation at the radius of the designated row, with the three blocks being the contributions from three adjacent radii (due to the three-point spatial differencing). In toroidal geometry the problem decouples into separate toroidal mode numbers n, but toroidal effects couple the various poloidal mode numbers m for each n. Now we obtain a separate matrix problem for each n: $L_n(\partial \tilde{X}_n/\partial t) = R_n \tilde{X}_n$, and using three-point difference formulas, L_n and R_n are again block tridiagonal matrices. Now, however, if $\tilde{X}_n$ is truncated to include M distinct poloidal components, each block matrix is $6M \times 6M$. We solve this system with the routine BTMS [12].

Equation (52) can be solved as an initial value problem. Alternatively, the problem can be posed as an eigenvalue problem:

$$\lambda L\tilde{X} = R\tilde{X}. \tag{53}$$

Again, the problem decouples into separate toroidal mode numbers n. For each n, the solution of Eq. (53) with largest real $\lambda > 0$ is the asymptotic solution of Eq. (52).

To solve the problem numerically, for each toroidal mode number n, we use the following iteration scheme:

$$\left(\hat{L} - \frac{\Delta}{2}\hat{R}\right) X^{l+1} = \left(\hat{L} + \frac{\Delta}{2}\hat{R}\right) X^{l}, \tag{54}$$

where l is the iteration number. Here $\hat{L}$ and $\hat{R}$ are the matrices resulting from expressing the operators L and R in centered finite difference form in ρ and taking a finite number M of poloidal Fourier components. The parameter Δ has the dimensions of time and will be normalized to the poloidal Alfvén time τ_{Hp}.

Choosing $\Delta \equiv \Delta t \lesssim t_{Hp}$, Eq. (54) is the full implicit time-stepping scheme that solves Eqs. (15)–(20) and is stated symbolically by Eq. (52). For larger values of Δ, it is an iteration scheme for solving Eq. (53), as will be shown below. Written in this way, we have the flexibility of studying both types of problems. This is important because this code is being generalized to include nonlinear terms. As the size of Δ is increased, the linear problem can be solved in an efficient manner.

Before considering the behavior with Δ of the iterative scheme of Eq. (54), let us discuss the implementation of the boundary conditions described in Section 3. In the solution of a system of second-order equations as a matrix problem, the two boundary conditions for each quantity are normally imposed with one at each end of the radial grid. Here we impose at the origin

$$\begin{aligned}
&\chi_{mn} = \alpha_{mn} = \Lambda_{mn} = 0, \\
&\psi_{mn} = \phi_{mn} = p_{mn} = 0 \qquad \text{for } m \neq 0, \\
&\frac{\partial \psi_{mn}}{\partial \rho} = \frac{\partial \phi_{mn}}{\partial \rho} = \frac{\partial p_{mn}}{\partial \rho} = 0 \qquad \text{for } m = 0.
\end{aligned} \tag{55}$$

At the edge we obtain ψ and χ from discretizing Eqs. (49) and (50) in a time-centered fashion and replacing Δt by Δ (Δ is only identical to the time differential Δt for small Δ). The resulting equations satisfy Eq. (47) when ϕ and Λ satisfy Eq. (48). Because the equation for α is first order, we choose simply to use a linear extrapolation boundary condition on α at the edge. The boundary condition for ϕ is obtained from Eq. (48), and Eq. (51) gives the pressure at the edge. To summarize the edge boundary conditions,

$$\begin{aligned}
&\psi_{mn}^{l+1} + \frac{\Delta}{2}\left[\frac{F_{\text{eq}}}{q}(m - nq)\,\phi_{mn}^{l+1} + n\alpha_{mn}^{l+1}\right] \\
&\quad = \psi_{mn}^{l} - \frac{\Delta}{2}\left[\frac{F_{\text{eq}}}{q}(m - nq)\,\phi_{mn}^{l} + n\alpha_{mn}^{l}\right], \\
&\chi_{mn}^{l+1} + \frac{\Delta}{2}\left[\frac{F_{\text{eq}}}{q}(m - nq)\,\Lambda_{mn}^{l+1} + m\alpha_{mn}^{l+1}\right] \\
&\quad = \chi_{mn}^{l} - \frac{\Delta}{2}\left[\frac{F_{\text{eq}}}{q}(m - nq)\,\Lambda_{mn}^{l} + m\alpha_{mn}^{l}\right], \\
&\alpha_{mn}^{l+1} = \text{linear extrapolation}, \\
&m\phi_{mn}^{l+1} = n\Lambda_{mn}^{l+1}, \\
&p_{mn}^{l+1} = 0.
\end{aligned} \tag{56}$$

Only the edge boundary condition on Λ remains to be established. For $m = 0$, Eq. (48) implies that $\Lambda_{0n} = 0$ at the edge. For $m \neq 0$, Eqs. (44) and (45) imply $\Lambda_{mn} \sim \rho^{|m|+1}$ as $\rho \to 0$, so that the second boundary condition for Λ may be expressed

$$\Lambda_{mn}\big|_{\rho = a} = 0 \qquad \text{for } m = 0$$

and (57)

$$\left.\frac{\partial \Lambda_{mn}}{\partial \rho}\right|_{\rho = 0} = 0 \qquad \text{for } m \neq 0.$$

For $m \neq 0$, Eq. (57) provides a second boundary condition on Λ at the origin rather than an edge boundary condition.

To solve Eq. (54) with the boundary conditions [Eqs. (55)–(57)], consider two solutions $\tilde{X}_a^{l+1}$ and $\tilde{X}_b^{l+1}$ to Eq. (54) for a given $\tilde{X}^l$, both of which satisfy the boundary conditions of Eqs. (55) and (56) although not necessarily Eq. (57) for $m \neq 0$. The boundary conditions for these solutions differ only in those applied for Λ_{mn} (with $m \neq 0$) at the edge. Defining $\tilde{X}^h = \tilde{X}_a^{l+1} - \tilde{X}_b^{l+1}$, we see that $\tilde{X}^h$ is a solution of the homogeneous equation

$$\left(L - \frac{\Delta}{2} R\right) \tilde{X}^h = 0 \tag{58}$$

with boundary conditions satisfying those of Eq. (55) at the origin and

$$\begin{aligned}
\psi^h_{mn} + \frac{\Delta}{2}\left[\frac{F_{\text{eq}}}{q}(m - nq)\,\phi^h_{mn} + n\alpha^h_{mn}\right] &= 0,\\
\chi^h_{mn} + \frac{\Delta}{2}\left[\frac{F_{\text{eq}}}{q}(m - nq)\,\Lambda^h_{mn} + m\alpha^h_{mn}\right] &= 0,\\
\alpha^h_{mn} &= \text{linear extrapolation},\\
m\phi^h_{mn} &= n\Lambda^h_{mn},\\
p^h_{mn} &= 0,
\end{aligned} \tag{59}$$

for specified Λ^h_{mn} $(m \neq 0)$ at the edge. For each $m \neq 0$, the homogeneous equation (58) admits an independent solution $\tilde{X}^{hm}$ with boundary conditions satisfying Eqs. (55) and (59) and having edge conditions on Λ

$$\Lambda^{hm}_{m'n} = m\delta_{mm'}. \tag{60}$$

For these solutions Eq. (59) takes the form

$$\begin{aligned}
\psi^{hm}_{m'n} &= -\frac{\Delta n}{2}\left[\frac{F_{\text{eq}}}{q}(m - nq)\,\delta_{mm'} + \alpha^{hm}_{m'n}\right],\\
\chi^{hm}_{m'n} &= -\frac{\Delta m'}{2}\left[\frac{F_{\text{eq}}}{q}(m - nq)\,\delta_{mm'} + \alpha^{hm}_{m'n}\right],\\
\alpha^{hm}_{m'n} &= \text{linear extrapolation},\\
\Lambda^{hm} &= n\delta\\
\phi^{hm}_{m'n} &= n\delta_{mm'},\\
p^{hm}_{m'n} &= 0.
\end{aligned} \tag{61}$$

These homogeneous solutions do not satisfy $\partial A_{m'n}/\partial\rho = 0$ at $\rho = 0$; rather, $A_{m'n} \sim \rho$ is observed. This behavior arises as a result of the form of the radial difference operations applied to A occurring in the definition of U^{θ} [Eq. (33)], where $\partial/\partial\rho\ [1/\rho\ \partial/\partial\rho\ (\rho A)] = 0$ for $A \sim \rho$.

Given that there are M (or $M-1$ if $m = 0$ is present) poloidal components of A which must satisfy $A_{mn} = 0$ and $\partial A_{mn}/\partial\rho = 0$ at $\rho = 0$ and that there are an equal number of independent homogeneous solutions to Eq. (58) having $\partial A_{mn}/\partial\rho \neq 0$ at $\rho = 0$, it is possible to add a linear combination of the homogeneous solutions to any solution of Eq. (54) to obtain another solution of Eq. (54) with the desired boundary conditions on A_{mn} at the origin. With this in mind, we are free to solve Eq. (54) subject to a conveniently imposed edge boundary condition for A and then to add the superposition of homogeneous solutions to guarantee the boundary condition (57). For this convenient boundary condition we choose $A_{mn} = 0$ at the edge. With this choice the edge boundary conditions of Eq. (56) become

$$\begin{aligned}
\psi_{mn}^{l+1} + \frac{n\Delta}{2}\alpha_{mn}^{l+1} &= \psi_{mn}^{l} - \frac{\Delta}{2}\left[\frac{F_{\text{eq}}}{q}(m-nq)\,\phi_{mn}^{l} + n\alpha_{mn}^{l}\right],\\
\chi_{mn}^{l+1} + \frac{m\Delta}{2}\alpha_{mn}^{l+1} &= \chi_{mn}^{l} - \frac{\Delta}{2}\left[\frac{F_{\text{eq}}}{q}(m-nq)\,A_{mn}^{l} + m\alpha_{mn}^{l}\right],\\
\alpha_{mn}^{l+1} &= \text{linear extrapolation},\\
\phi_{mn}^{l+1} &= A_{mn}^{l+1} = p_{mn}^{l+1} = 0.
\end{aligned} \tag{62}$$

The overall solution strategy is described then in the following:

(1) At the outset of the calculation, obtain the homogeneous solutions X^{hm} to Eq. (58) with the boundary conditions of Eqs. (55) and (59), with one solution for each $m \neq 0$. This step is executed only once.

(2) Given X^{l}, solve the inhomogeneous Eq. (54) for $X^{i(l+1)}$ with the boundary conditions of Eqs. (55) and (62).

(3) To the solution $X^{i(l+1)}$ of the inhomogeneous equation, add a linear combination $\sum_{m\neq 0} c_m X^{hm}$ of the homogeneous equation solutions with the coefficients c_m determined, such that

$$X^{l+1} = X^{i(l+1)} + \sum_{m\neq 0} c_m X^{hm}$$

satisfies the boundary condition [Eq. (57)] for A.

(4) If X^{l+1} is not a converged eigenfunction, increment l, return to step (2) and iterate.

Having described the details of the iterative scheme, we consider the behavior as the convergence parameter Δ is varied. We assume that the problem

$$\lambda \hat{L} X = \hat{R} X \tag{63}$$

has a complete set of eigenfunctions X_j with real eigenvalues λ_j and, further, that the eigenfunctions are nondegenerate, so that $\lambda_j \neq \lambda_{j'}$ for $j \neq j'$. Then, any solution vectors $\tilde{X}^l$ and $\tilde{X}^{l+1}$ can be written as linear combinations $\tilde{X}^l = \sum_j c_j^l X_j$ and $\tilde{X}^{l+1} = \sum_j c_j^{l+1} X_j$ of X_j. Substituting into Eq. (54), applying $\hat{L}^{-1}$, and invoking the independence of X_j, we obtain

$$c_j^{l+1} = \left(\left(1 + \frac{\Delta}{2}\lambda_j\right)\Big/\left(1 - \frac{\Delta}{2}\lambda_j\right)\right) c_j^l. \qquad (64)$$

Hence, the iterative scheme will pick out and converge to the eigenfunction X_j for which $|(1 + \Delta/2\,\lambda_j)/(1 - \Delta/2\,\lambda_j)|$ is a maximum. Furthermore, the rate of convergence is very rapid when $|(1 + \Delta/2\,\lambda_j)/(1 - \Delta/2\,\lambda_j)|$ is large (i.e., when $\Delta \approx 2/\lambda_j$). This is illustrated in Fig. 1 where the number of iterations to converge a $(m = 1; n = 1)$ tokamak eigenfunction in cylindrical geometry is plotted as a function of Δ. The eigenvalue for this case is $\lambda = 0.14\tau_{H_p}^{-1}$, which is consistent with $\Delta \approx 14\tau_{H_p}$ for the fastest convergence. The eigenvalues are calculated as follows: the quantities λ_i^l are defined by

$$\lambda_i^l = \frac{(\hat{R}X^l)_i}{(\hat{L}X^l)_i}, \qquad (65)$$

where i is the index for the vector component and ( ) indicates an average over ρ. When the numerical scheme converges to an eigenfunction, λ_i^l becomes independent of l and i and defines the eigenvalue λ.

An interesting consequence of Eq (64) is the ability to calculate a spectrum of eigenfunctions simply by varying the convergence parameter Δ. We assume that λ_i and λ_j are adjacent eigenvalues (i.e., that no eigenfunctions have intermediate eigenvalues). When $\Delta \approx 2/\lambda_i$, the solution converges rapidly to X_i, and when $\Delta \approx 2/\lambda_j$, the

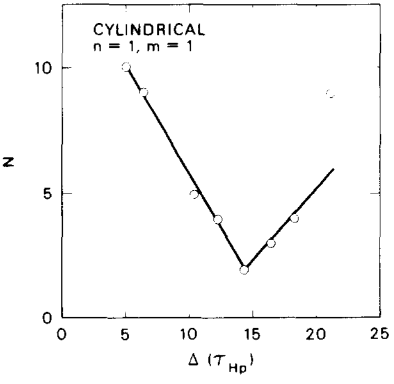

FIG. 1. Number of steps (N) to converge as a function of iteration step size Δ. Less than ten steps are required over a wide range of Δ.

solution converges rapidly to X_j. Assuming $\lambda_j > \lambda_i$, there is an intermediate transition value of Δ such that

$$\left|\left(1+\frac{\Delta}{2}\lambda_j\right)\Big/\left(1-\frac{\Delta}{2}\lambda_j\right)\right| = \left|\left(1+\frac{\Delta}{2}\lambda_i\right)\Big/\left(1-\frac{\Delta}{2}\lambda_i\right)\right|.$$

Choosing the $-$ sign on the left $(\Delta/2\,\lambda_j > 1)$ and the $+$ sign on the right $(\Delta/2\,\lambda_i < 1)$ and solving, we obtain

$$\Delta_{ij}^{\mathrm{tr}} = 2/\sqrt{\lambda_i \lambda_j} \tag{66}$$

for this transition value. This is illustrated in Fig. 2 where the $(m = 1; n = 1)$ eigenfunctions for the cylindrical tokamak configuration used in Fig. 1 are calculated as Δ is varied. The eigenvalues show discrete transitions at the appropriate values of Δ as marked by the arrows. The poloidal components of the velocity for each of the eigenfunctions are shown in the insets. The ρ component of the velocity has no nodes for the largest λ, one node for the second largest and two for the third largest. This is typical behavior for the most unstable, second-most unstable and

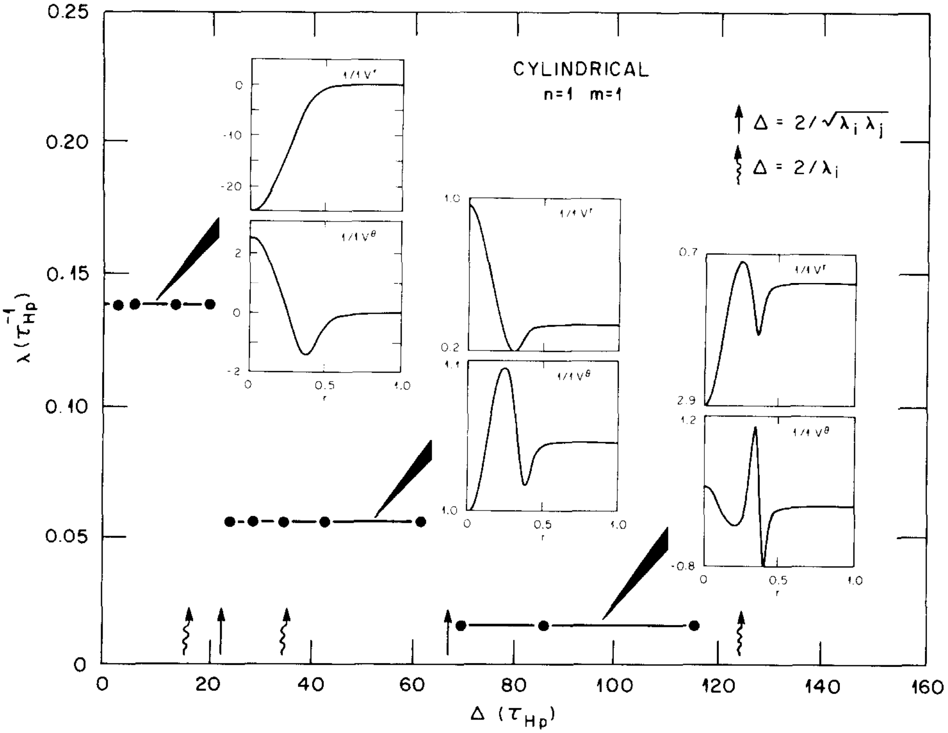

FIG. 2. Eigenvalue λ as a function of Δ. The iteration of Eq. (54) selects an eigenvalue and corresponding unstable eigenfunction, depending on Δ.

third-most unstable modes. This is, in fact, what is being selected by the choice of Δ. Also shown for reference are the resonant values of Δ for each mode.

Before leaving the subject of the calculation of eigenfunctions and eigenvalues, it is worthwile to compare the eigenvalues of the iterative scheme with the growth rates normally measured using initial value codes. Equation (64) shows that for $\Delta/2\,\lambda_j > 1$, the iteration procedure flips the sign of the growing solution. Asymptotically a growing solution will exhibit the growth rate γ_j, defined by

$$\pm\exp(\gamma_j\Delta)=\left(1+\frac{\Delta}{2}\lambda_j\right)\Big/\left(1-\frac{\Delta}{2}\lambda_j\right)=\frac{c_j^{l+1}}{c_j^{l}}, \tag{67}$$

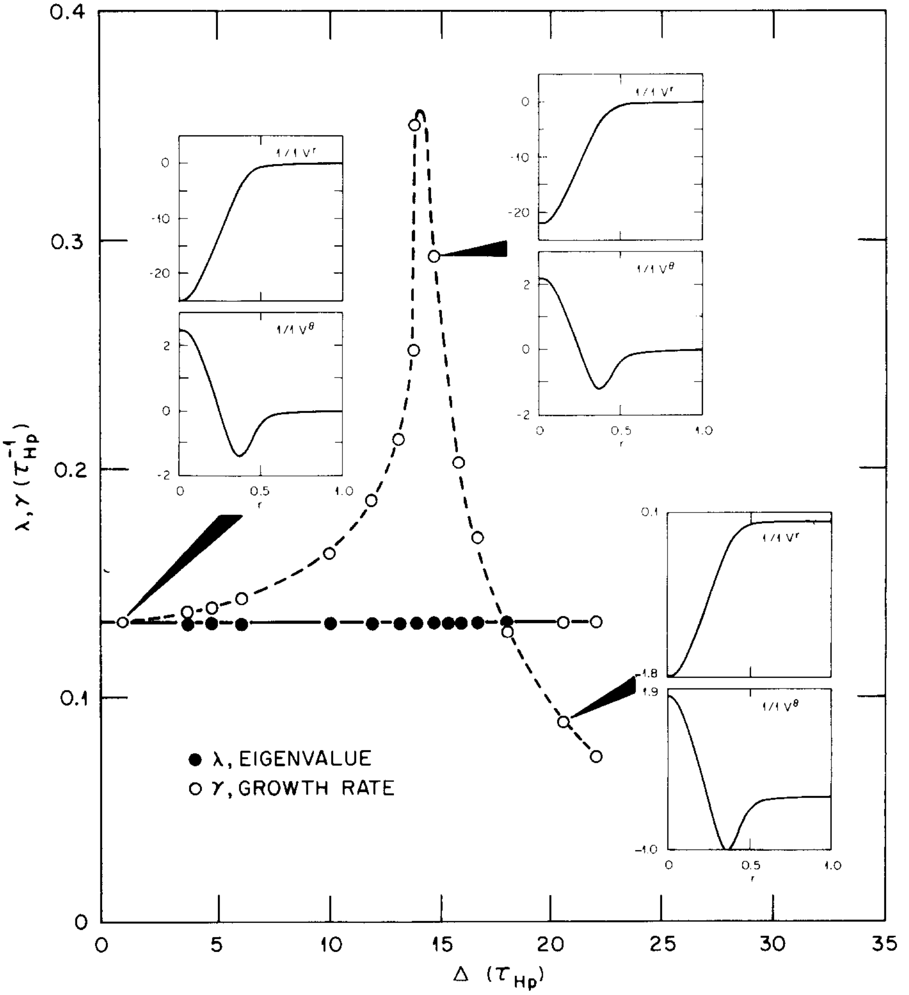

FIG. 3. The eigenvalue (λ) and eigenfunctions do not vary with Δ between transitions. The growth rate (γ) agrees with λ for small Δ. The most unstable mode is illustrated.

so that

$$\gamma_j = \frac{1}{\Delta} \ln\left(\left(1 + \frac{\Delta}{2} \lambda_j\right) \Big/ \left(1 - \frac{\Delta}{2} \lambda_j\right)\right). \tag{68}$$

Such growth rates are normally used in initial value codes to measure the growth of the perturbations as well as the linear eigenvalues when nonlinear effects are unimportant. Equation (67) shows that for $\Delta\lambda_j \ll 1$, $\gamma_j \approx \lambda_j \approx (1/\Delta) \ln(c_j^{l+1}/c_j^l)$, giving good agreement between the growth rate and the eigenvalue in the limit of small Δ. In the limit $\Delta \to 0$ (i.e., $\Delta\lambda_j \ll 1$ for all λ_j), Eq. (64) shows that the selected eigenfunction is that with the largest eigenvalue, and Eq. (67) shows that the initial value calculation of the growth rate gives that eigenvalue. For the incompressible model used here, we expect all eigenvalues to satisfy $\lambda_j \lesssim \tau_{H_p}^{-1}$, so that for $\Delta \ll \tau_{H_p}$ the parameter Δ is equivalent to a time step-size. This will be true whenever $\Delta\lambda_j \ll 1$ for the fastest growing eigenfunction. To illustrate the behavior of the growth rate γ as Δ is varied, Fig. 3 shows λ and γ plotted versus Δ for the same cases as Fig. 1. Note that Δ falls in the range that gives the largest eigenvalue shown in Fig. 2. The resonant behavior of γ at $\Delta = 2/\lambda$, the approach of γ to λ as $\Delta \to 0$, and the constancy of λ as Δ is increased are all clearly shown. The plotted values of γ were obtained by calculating the actual growth of the eigenfunction in the calculations. These values are seen to obey Eqs. (67) and (68) very well using the corresponding 2 and λ, thus supporting the validity of this analysis. Finally, the insets show the poloidal components of the velocity for three different values of Δ, with the good agreement indicating the independence of the result from the particular choice of Δ within the range of convergence to the particular eigenfunction obtained.

V. APPLICATION TO THE $n = 1$ MODE IN TOKAMAKS

We now apply the fully implicit iterative scheme to the calculation of the $n = 1$ mode for the tokamak configuration. Two sequences are considered. In the first, for toroidal geometry we consider a configuration with aspect ratio $A_R = 4$ and several equilibria of various beta, all having safety factor profiles with the range $0.9 = q_0 \leqslant q(\rho) \leqslant q_a = 2.3$ from the magnetic axis to the edge. The pressure profile is taken to vary as $p \propto \psi^2$. The dominant poloidal component for these cases is $m = 1$. The second sequence consists of cylindrical geometry calculations for an equilibrium having a constant equilibrium toroidal magnetic field $B_{\mathrm{eq}}^{\zeta} = 1$ and a safety factor profile $0.9 = q_0 \leqslant q(\rho) \leqslant q_a = 3.3$. Here, the $m = 0 - 3$ components are considered separately. For the toroidal calculations, comparisons are carried out with the results of the ideal MHD stability code ERATO [9], which is based on an energy principle, and with the results of the initial value resistive MHD code RST [6], which uses reduced equations. In cylindrical geometry, comparison is made with the results of the initial value resistive MHD code CYL [8], which uses the full equations.

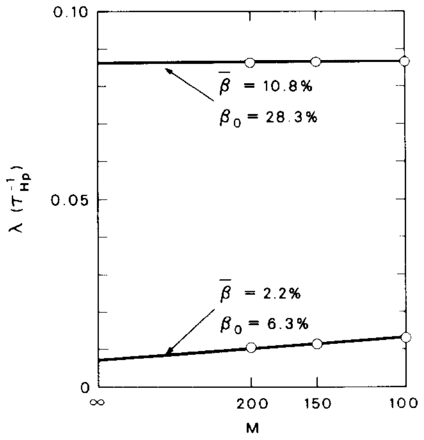

FIG. 4. Convergence of λ with number of radial grid points (M). The scale is M^{-2} [illegible]

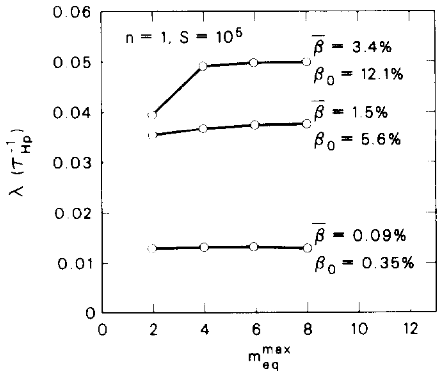

FIG. 5. Convergence with number of equilibrium Fourier modes.

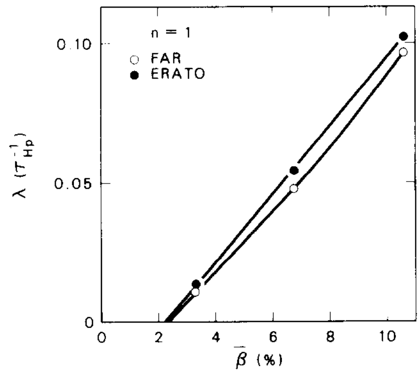

FIG. 6. Comparison of ideal results with the code ERATO [9].

Accurate results must be converged both in the number of grid points used in ρ and in the number of Fourier modes retained in the expansions of both the dynamic and equilibrium quantities. In Fig. 4, the $n=1$ eigenvalue is shown as a function of the number of radial grid points for two cases in the toroidal sequence. For large $\lambda(\sim 0.1\tau_{H_p}^{-1})$, results are converged with ~ 100 grid points. For smaller $\lambda(\sim 0.01\tau_{H_p}^{-1})$, however, a convergence study is required with the results extrapolated to an infinite number of points. Figure 5 shows the convergence behavior when varying the number of modes used to describe the equilibrium. The required number of modes (for errors of $\leqslant 1\%$ in λ) increases from a few at small beta, where the distortion of flux surfaces is small, up to 5 to 10 modes for larger beta, where flux surfaces are significantly distorted. For the $n=1$ results presented in this paper, dynamic modes from $m=-1$ to $m=4$ are used and have been determined to give errors of $\lesssim 1\%$. For the safety factor considered here $(0.9 \leqslant q \leqslant 2.3)$, this distribution of modes covers the resonant region with two additional modes above and below.

In Fig. 6, a comparison of the ideal toroidal results with those of the ideal MHD stability code ERATO [9] is shown. The agreement is excellent. The $n=1$ mode structure in both sets of results is that of an $m=1$ dominated internal

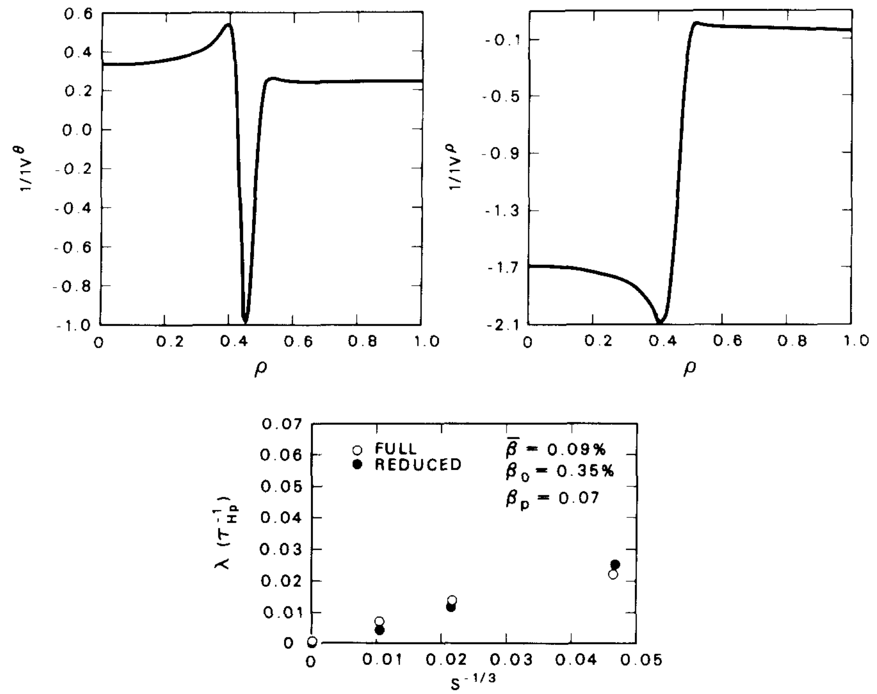

FIG. 7. Comparison of results using the full equations (FAR code) with the results obtained with the reduced equations (RST code). Stability results for $n=1$ and $\beta_0=0.35\%$. The mode structure is shown only for the energetically dominant $m/n=1/1$ component.

kink. This is expected due to the presence of the $q = 1.0$ surface in the equilibria used. In the FAR code, for purposes of this comparison, the resistivity was set to zero.

Resistive calculations were also carried out for the toroidal sequence and comparisons made with the results of the reduced equations using the code RST. In Figs. 7, 8, and 9 the calculated eigenvalues for equilibria having different beta are shown, using both the reduced and full equations. The eigenvalues are shown as functions of $S^{-1/3}$ (S is the ratio of resistive to poloidal Alfvén times). Also shown is the structure of the velocity vector in the poloidal plane as obtained with the full equations. The equilibrium used for the results shown in Fig. 7 had the lowest beta value ($\bar{\beta} = 0.09\%$). The eigenvalues found using the two sets of equations are virtually identical. The poloidal velocity structure is that of a resistive tearing mode. The resistive nature of the mode implies that in the ideal limit ($S \to \infty$) the mode should be stable, as seen in Fig. 7.

In Fig. 8, comparative stability results are shown for an equilibrium with higher beta ($\bar{\beta} = 2.4\%$). The eigenvalues from the two sets of equations differ significantly, with the reduced equations giving a purely resistive mode and the full equations an ideally unstable mode. The poloidal velocity structure (at the top of the figure) is

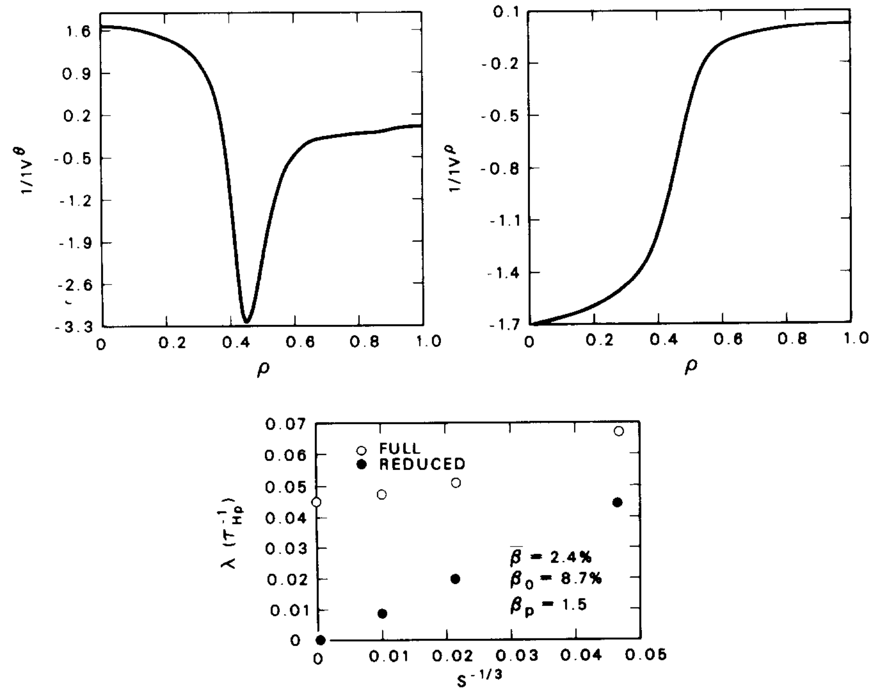

FIG. 8. Stability results for $n = 1$ and $\beta_0 = 8.7\%$. At this β_0, the internal kink mode is unstable. The FAR result obtains this intability, but it is ordered out of the reduced equations. The mode structure is shown only for the energetically dominant $m/n = 1/1$ component.

that of an internal kink. As is well known, the ordering scheme used to derive the reduced equations excludes the internal kink driving terms in lowest order. Thus, the difference in Fig. 8 is anticipated. The structure of the mode produced by the reduced equations is that of a resistive ballooning mode [6].

In Fig. 9, results using a high-beta equilibrium are presented. Again, the agreement between the full and reduced equations is excellent. The mode structure is that of a resistive ballooning mode that is adequately treated with the reduced equations. This equilibrium lies in the second stability region of the ideal internal kink, which is detailed in other work [13, 14]. Thus, the reduced and full equations give results for $n=1$ that agree very well at high and low beta. They differ, however, at intermediate beta, where such differences are expected due to the presence of the internal kink mode.

Finally, the cylindrical geometry eigenvalues for $m=0-3$ obtained from FAR are compared in Fig. 10 to those from the full-equations, initial-value MHD code CYL [8]. Again, the agreement is excellent.

In summary, the fully implicit scheme described here provides linear eigenfunctions and eigenvalues in good agreement with those obtained by other methods when agreement is anticipated. Comparisons have been carried out for a considerable range of cases with (1) an ideal stability model using an energy-principle

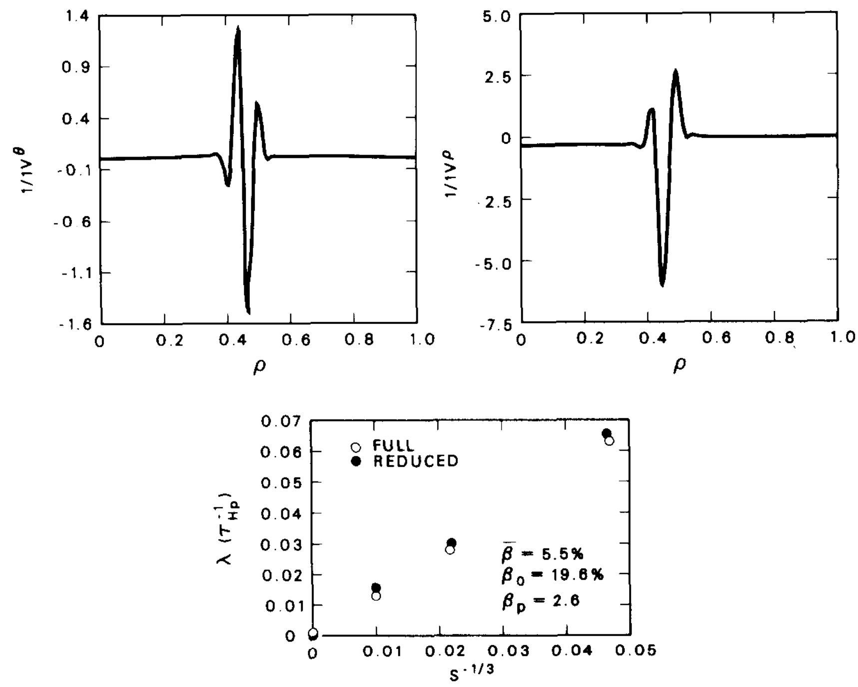

FIG. 9. Stability results for $n=1$ and $\beta_0=19.6\%$. The mode structure is shown only for the energetically dominant $m/n=1/1$ component.

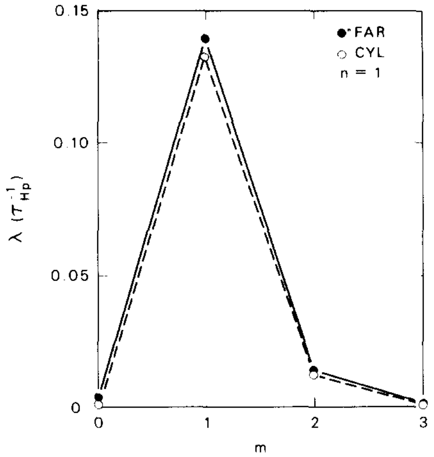

FIG. 10. Comparison of FAR, run in the cylindrical limit, with the cylindrical code CYL [8].

approach, (2) a reduced-equations model using a semi-implicit numerical scheme, and (3) a full-equations model using a semi-implicit scheme and advancing **v** and **B** rather than potential functions. In all cases the fully implicit scheme of the FAR code produced results in significantly less computer time than used by the codes with which it was compared. The efficiency of this scheme is due to the small number of iterations required for the rapid convergence to an eigenfunction (see Fig. 1).

VI. DISCUSSION AND CONCLUSIONS

The full set of resistive MHD equations, together with an incompressibility assumption, gives a tractable set of equations to be solved numerically. The linear implementation of these equations using a fully implicit scheme utilizes a superposition of the homogeneous and inhomogeneous solutions of the system of equations in order to impose the edge boundary conditions and have regular behavior at the origin. The numerical scheme allows extremely rapid convergence through selection of values for the convergence parameter Δ, which may be identified with the time step when Δ is small. Therefore, converged eigenvalues and eigenfunctions may be found in very few steps if an approximate value for the eigenvalue is known. This would be the case in a parameter scan, once λ for a "neighboring" case has been determined. Another advantage of this numerical scheme is that it allows the study of modes other than the most unstable one. This scheme is being extended to solve the nonlinear set of MHD equations.

REFERENCES

1. M. AZUMI *et al.*, *in* "Proceedings of the U.S.–Japan Workshop on 3-D MHD Simulation," Nagoya, Japan, 1983.
2. D. SCHNACK AND J. KILLEEN, *J. Comput. Phys.* **35** (1980), 110.
3. T. C. HENDER AND D. C. ROBINSON, *Comput. Phys. Commun.* **24** (1981), 413.
4. A. AYDEMIR AND D. C. BARNES, "Proceedings of the U.S.–Japan Theory Workshop on 3-D MHD Studies for Toroidal Devices," p. 187, Oak Ridge National Laboratory, Oak Ridge, Tennessee, 1981.
5. R. IZZO, D. A. MONTICELLO, H. R. STRAUSS, W. PARK, J. MANICKAM, R. C. GRIMM, AND J. DELUCIA, *Phys. Fluids* **26** (1983), 3066.
6. J. A. HOLMES, B. A. CARRERAS, H. R. HICKS, V. E. LYNCH, AND K. E. ROTHE, *Phys. Fluids* **25** (1982), 800; V. E. LYNCH, B. A. CARRERAS, H. R. HICKS, J. A. HOLMES, AND L. GARCIA, *Comput. Phys. Commun.* **24** (1981), 465.
7. H. R. STRAUSS, *Phys. Fluids* **20** (1977), 1354.
8. J. A. HOLMES, B. A. CARRERAS, T. C. HENDER, H. R. HICKS, V. E. LYNCH, AND B F. MASDEN, *Phys. Fluids* **26** (1983), 2569.
9. R. GRUBER, F. TROYON, D. BERGER, L. C. BERNARD, S. ROUSSET, R. SCHREIBER, W. KERNER, W. SCHNEIDER, AND K. V. ROBERTS, *Comput. Phys. Commun.* **221** (1981), 323.
10. T. C. HENDER, B. A. CARRERAS, W. A. COOPER, J. A. HOLMES, P. H. DIAMOND, AND P. L. SIMILON, *Phys. Fluids* **27** (1984), 1439.
11. H. R. HICKS, B. CARRERAS, J. A. HOLMES, D. K. LEE, AND B. V. WADDELL, *J. Comput. Phys.* **44** (1981), 46.
12. A. C. HINDMARSH, "Solution of Block-Tridiagonal Systems of Linear Algebraic Equations," Lawrence Livermore Laboratory Report UCID-30150, 1977.
13. G. B. CREW AND J. J. RAMOS, "Asymptotic Theory of the Internal Kink Mode in Current Carrying Toroidal Plasmas," MIT Report, No. PTP-82/2, MIT Press, Cambridge, Mass., 1982.
14. J. MANICKAM, "Stability of $n=1$ Internal Modes in Tokamaks," Princeton Plasma Physics Laboratory Report, No. PPPL-2064, 1983.